COMMUNICATIONS IN COMPUTATIONAL PHYSICS
Vol. **2**, No. 4, pp. 640-661

Commun. Comput. Phys.
August 2007

# Simulation of Liquid Metal Droplets from Field Emission

Anton VanderWyst[1,*], Andrew Christlieb[2], Mark Sussman[3] and Iain D. Boyd[4]

[1] *Raytheon Missile Systems, 1151 E. Hermans Road, P.O. Box 11337, Tucson, AZ 85734, USA.*
[2] *Department of Mathematics, Michigan State University, East Lansing, MI 48824, USA.*
[3] *Department of Mathematics, Florida State University, Tallahassee, FL 32306, USA.*
[4] *Department of Aerospace Engineering, University of Michigan, Ann Arbor, MI 48109, USA.*

Received 19 September 2006; Accepted (in revised version) 28 November 2006

Available online 8 January 2007

**Abstract.** Liquid metal droplets are accelerated by electrostatic forces in a process known as field emission. In this study, we simulate the emission of charged indium droplets on a needle in 2D cylindrical coordinates. The boundary element method is used to rapidly and accurately calculate the electric field on the fluid surface, which is then advected forward in time using level sets. This is the first time these methods have been combined, and this combination addresses difficult detachable surface tracking issues successfully. A histogram of droplet charge-to-mass ratio is generated in which it is predicted that smaller satellite droplets are more densely charged. In addition, our model is compared with independent pre- and post-snap off data and produces good agreement with the result.

**AMS subject classifications**: 65C20, 65M06, 65N38, 65Z05, 74S15, 76B45, 81T80

**PACS (2006)**: 47.11.-j, 47.11.Hj, 79.70.+q

**Key words**: Field emission electric propulsion, modeling, level set, boundary element method.

## 1 Introduction

Field emission refers to the process of using a strong electric field to produce a spray of charged liquid droplets or ions. The field comes from a potential difference between an electrode and the liquid surface that is balanced by the surface tension of the fluid. As

*Corresponding author. *Email addresses:* Anton_Vanderwyst@raytheon.com (A. VanderWyst), christlieb@math.msu.edu (A. Christlieb), sussman@math.fsu.edu (M. Sussman), iainboyd@umich.edu (I. D. Boyd)

 

a result, the surface deforms to an equilibrium shape of a cone. The strong field at the tip then causes a propellant jet to form [1]. The phenomenon of droplet and ion evaporation from charged liquid surfaces is of considerable interest in many areas of science and technology. Some of the many realms in which field emission occurs include: electron microscopy, data displays, carbon nanotube fluorescence, ink jets and thermoelectric coolers.

Field emission thrusters are currently considered for a variety of space missions both in the United States and Europe. FEEP thrusters provide a source of high specific impulse, ultra-low impulse bit electrostatic space propulsion. A space-tested indium FEEP has been under development in Austria for over a decade [2]. The liquid metal ion source (LMIS) base consists of a needle covered in the element indium reacting to an applied electric potential from an extractor ring held above the tip at -6 kV. When the field strength at the tip reaches $10^9 V/m$, indium is then ionized from the surface and accelerated over a fine tungsten needle that is about 1 cm long and 50 $\mu$m wide. Depending on the mass flow rates, either ions or droplets are observed to be emitted from the tip. A schematic of a FEEP thruster [3] is shown in Fig. 1.

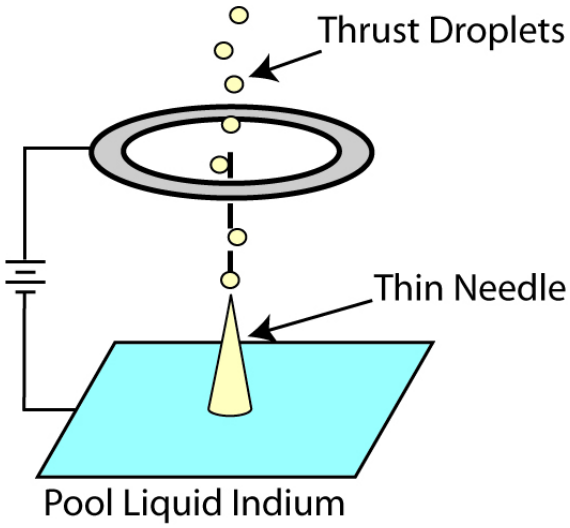


Figure 1: FEEP in droplet production mode.

The existence and corresponding behavior of droplets is of large practical concern in FEEP because as more droplets form, operational efficiency decreases, lifetime is limited due to the electrode clogging and plume divergence is unpredictable due to varying charge distributions. Therefore, a numerical investigation into the formation and charge of these expelled droplets has been undertaken. Experimental efforts indicate that below 20 $\mu$A only ion emission occurs in FEEP needles [4]. Above that point, at a current that varies based on the thermal and electrical properties of the fluid, periodic stochastic motions of droplet formation and emission interrupt the steady ion stream.

As the potential on the ring electrodes increases, the liquid curvature increases until

reaching a conical surface with a half angle of 49°, a so-called *Taylor cone* where the forces of electrostatics and surface tension are mathematically in balance [5]. During droplet formation and detachment, the fluid radius necks to zero width between the two shapes. When simulating snap off, this can cause substantial surface location and divide-by-zero difficulties. A combination of the level set and the boundary element methods successfully sidesteps this issue.

Level sets are one mathematical method used to computationally track the movement of a surface between solid-liquid, liquid-vacuum and other types of discrete interfaces. They were introduced by Osher and Sethian [6] and have been heavily studied over the next couple of decades. A complementary surface simulation technique is the boundary element method (BEM). Using boundary points in simulations mimics the more common finite element method, except that boundary elements span only the edges of the shapes instead of the entire volume. This allows for faster computation due to use of fewer nodes, avoids the need to adaptively mesh, allows for easier design changes and successfully deals with infinite domains and arbitrary shapes.

This paper has two main objectives. The first is to explain how the level set and boundary element methods are coupled to simulate liquid metal droplets, while the second goal is to predict droplet size and charge characteristics and relate them to external work. This study discusses how these two mathematical techniques can be used on a new topic, examines some of the computational difficulties inherent in surface tracking and models how a field emitter shape changes over time. The paper is organized as follows. Section 2 presents the physical model governing equations. Section 3 describes how the level set and boundary element methods are formulated and why they are appropriate to solve these evolution equations. Section 4 presents illustrative results on droplet size and charge.

## 2 Overview

### 2.1 Model description

The simulation model considers an incompressible, isothermal and viscous liquid against a perfect vacuum. The propellant indium is treated as a perfect conductor and its atoms are accelerated with ring electrodes, producing thrust. The 2D axisymmetric governing equation for the system is

$$\begin{aligned} &\frac{1}{r}\frac{\partial}{\partial r}(rv_r)+\frac{\partial v_z}{\partial z}=0, \\ &\frac{\partial \mathbf{A}}{\partial t}+\left(v_r\frac{\partial}{\partial r}+v_z\frac{\partial}{\partial z}\right)\mathbf{A}=\mathbf{B}+\sigma\kappa+qE_n. \end{aligned} \tag{2.1}$$

The electric field $\vec{E}$ is treated as a surface normal force $E_n$, since all electrons in a conductor remain on the surface. Continuity and conservation of momentum are enforced. The

main momentum equation state terms are

$$\mathbf{A}=\begin{bmatrix} v_r \\ v_z \end{bmatrix}, \quad \mathbf{B}=\begin{bmatrix} -\frac{1}{\rho}\frac{\partial p}{\partial r}+\nu\left(\nabla^2 v_r-\frac{v_r}{r^2}\right) \\ -\frac{1}{\rho}\frac{\partial p}{\partial z}+\nu\nabla^2 v_z \end{bmatrix}. \tag{2.2}$$

The normal stress boundary condition at the free surface is

$$p=\sigma\kappa+qE_n+2\mu(D_{liquid}\cdot\vec{n})\cdot\vec{n}, \tag{2.3}$$

where $D$ is the rate of deformation tensor. The electric field is computed by $\vec{E}=-\nabla U(\vec{x})$, where $U(\vec{x})$ is the electrostatic potential at position $\vec{x}$.

## 2.2 Physical submodels

The surface tension $\sigma$ of liquid indium does not vary rapidly with temperature, as indicated by

$$\sigma_{In}=\frac{555-0.12(T[K]-430)}{1{,}000}\left[\frac{N}{m}\right]. \tag{2.4}$$

During normal FEEP operation, the temperature remains within the narrow operational range of 440-450 $K$ where indium is far enough above its melting point to be fully liquid [4]. The ability of indium to flow over a solid surface is determined largely by its viscosity $\mu$, which varies with temperature through the weak exponential relationship of

$$\mu_{In}=3\times10^{-4}e^{800/T[K]}\left[\frac{kg}{m\cdot s}\right]. \tag{2.5}$$

Over the expected temperature range, the fluid viscosity changes only 4%. The density $\rho$ of indium is given by

$$\rho_{In}=1{,}000\times(7.1295-6.7987\times10^{-4}(T-273.15))\left[\frac{kg}{m^3}\right], \tag{2.6}$$

and changes about 0.01% per degree Celsius.

Among the model assumptions, the treatment of the propellant as a perfect conductor is very reasonable. Since indium is a metal, the conductivity is so high that an electron can travel through the liquid surface along the needle body at the Fermi velocity. For metals, the Fermi energy ($e_F$) provides the minimal energy for conducting electrons. However, the maximum amount of energy which can be given to any electron is on $\mathcal{O}(\mu eV)$, so only the electrons very near the Fermi energy can participate in conduction [7]. The Fermi velocity ($v_F$) of these conduction electrons can be calculated from the Fermi energy. For indium, $v_F$ is

$$v_F=c\sqrt{\frac{2e_F}{m_e c^2}}=1.74\times10^6\left[\frac{m}{s}\right]. \tag{2.7}$$

The fluid flows at a maximum speed 10 orders of magnitude slower, only $1\times10^{-4}m/s$. The isothermal assumption for droplets is accurate because only radiation is available to cool them after snap off. For example, detachment occurs in 0.1 $\mu$s, but a 100 $\mu$m diameter droplet at 450 $K$ treated as a blackbody cools less than 0.1 $mK$ in that time. Therefore, $\sigma$, $\mu$ and $\rho$ can accurately be treated as constant.

# 3 Numerical methodology

When computationally tracking the movement of a surface between solid-liquid and liquid-vacuum interfaces as discussed in Section 2, the determination of the normal electric field commonly is quite drawn out and error-prone. The combination of the level set and the boundary element methods improves on prior work by providing similar or better resolution combined with a rapid simulation of droplet pinch off.

## 3.1 Level sets method

Interface tracking using level set computation relies on the determination and evolution of the surface boundary. In our model, the position of the free surface is updated via the level set equation

$$\phi_t+\vec{v}\cdot\bigtriangledown\phi=0, \tag{3.1}$$

where $\phi$ is the level set function; positive in liquid and negative in the vacuum. The interface velocity $\vec{v}$ is the indium fluid velocity. In the vacuum, lines of constant $\vec{v}$ are projected normal to the indium surface. The interface is advected by only the normal velocity component of $\vec{v}$. This component is the normalized gradient of the level set surface,

$$\vec{v_n}=\frac{\vec{v}\cdot\nabla\phi}{|\nabla\phi|}. \tag{3.2}$$

The extension was first suggested in [8], analyzed carefully in [9], and further discussed in [10, 11]. In the special case where $\vec{v_n}$=1, then Eq. (3.1) becomes a Hamilton-Jacobi equation whose solution generally develop kinks, or jumps in derivatives.

If a point starts on the surface $\partial\Omega$ where $\phi=0$, that particle moves through time, but remains on the surface. Fig. 2 shows the $\phi\geq0$ cross-section of a double-humped shape intersected at 3 different heights.

After each time step, $\phi$ is renormalized to be the signed distance function $d$. A signed distance function is an implicit function $\phi$ with $|\phi(\vec{x})|=d(\vec{x})$ for all $\vec{x}$. Connecting any point $\vec{x}$ with the nearest point $I$ on the surface boundary $\partial\Omega$ gives the path of steepest descent for $d$. Due to the reinitialization step, the distance constraint $|\nabla\phi|=1$ applies. The extrapolation procedure uses the distance function since $x_I=x-(\nabla\phi)\phi$ is the closest corresponding point on the interface. The curvature of the interface $\kappa$ can then be described

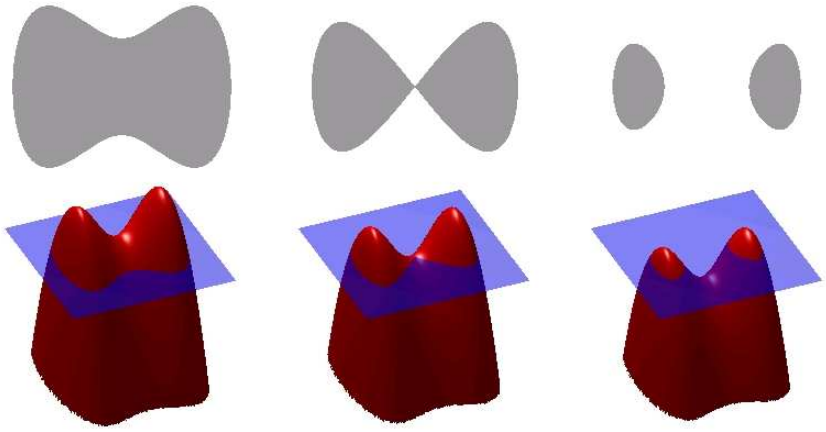

Figure 2: Level set surface determination at various heights.

using the level set variable $\phi$ itself as

$$\kappa = \frac{\nabla \cdot (\nabla \phi)}{|\nabla \phi|}. \tag{3.3}$$

Near pinch off, the curvature determination is more prone to errors as a greater change in $\kappa$ occurs within a smaller area. To combat this problem, adaptive mesh refinement is used to locally generate more cells in a given area, so that the surface curvature per cell is limited.

The free surface is represented with second order accuracy in space through a "coupled level set and volume-of-fluid" (CLSVOF) method. In addition to solving the level set equation, the volume-of-fluid function $V_F$ is computed [12, 13],

$$\frac{\partial V_F}{\partial t} + \vec{v} \cdot \nabla V_F = 0, \tag{3.4}$$

where the net volume of fluid is conserved both locally and globally. Interfaces are tracked in this volume-of-fluid method by locally calculating the flux of volume in or out of a given computational cell. If a cell has no fluid, $V_F = 0$; totally filled grid points have $V_F = 1$. Interface ('mixed') cells have $V_F \in (0,1)$ [14]. The cell (i,j) fluid volume fractions are determined by checking for fluid at points (x,y) via

$$V_F(x,y) = \begin{cases} 1 & \text{if fluid at } (x,y), \\ 0 & \text{if no fluid at } (x,y). \end{cases} \tag{3.5}$$

These local fluid values are combined with $H$, the Heaviside function evaluated as

$$V_{F_{ij}} = \frac{1}{\Delta x \Delta y} \int_i \int_j V_F(x,y)\, dx\, dy. \tag{3.6}$$

Using the above definitions for level sets, this work builds on prior two- and three-dimensional efforts of interface migration by Sussman [15]. A variety of numerical algorithm schemes are needed in the CLSVOF approach [16]. The method is briefly outlined below [17].

**1**. Advance the location of the interface using the coupled level set and volume of fluid method. Velocity and pressure fields are computed based on variable density projection methods [18].

**2**. Calculate nonlinear advective force terms in each fluid separately using high order, upwind, slope limited discretization. The liquid indium is discretized using a Godunov second-order upwind predictor-corrector step [19].

**3**. Compute the viscous forces. Use the Crank-Nicholson [20] and Runge-Kutta methods. The new velocity field is continuous across the $\phi=0$ surface. Surface tension is included as a body force, as in [21]. Curvature is calculated directly from volume fractions.

**4**. Cell centered forces are interpolated to face centered forces.

**5**. Pressure and velocity fields are updated and implicitly projected via

$$\begin{aligned} \nabla\cdot\frac{\nabla p}{\rho}&=\nabla\cdot v,\\ u&=v-\frac{\nabla p}{\rho}. \end{aligned} \tag{3.7}$$

The new velocity field satisfies the continuity condition and the new pressure satisfies the appropriate jump conditions $[p]=g$ and $[\frac{1}{\rho}\nabla p\cdot\vec{n}]=$h. The Cartesian-grid approach is used to approximate the divergence operator.

**6**. The liquid velocity is extrapolated in a narrow band around the $\phi=0$ interface.

**7**. Face centered velocity is interpolated back to cell centered velocities.

**8**. Finally, the cell centered pressure gradient term is updated.

### 3.2 Boundary element method

For all the benefits of surface determination, the efficient calculation of the magnitude of the normal electric field $E_n$ in Eq. (2.3) still presents many challenges. The algorithm employed in this study for determining the electrostatic force is the boundary element method (BEM).

The boundary element method rapidly and directly solves for the force on the surface without meshing the volume of the domain. It handles arbitrary geometries by only discretizing points along the boundary. For example, consider Poisson's equation

$$\triangle U(\overline{x})=-\frac{\breve{\rho}}{\epsilon_0},\quad \overline{x}\in\Omega,\qquad U|_{\partial\Omega}=f\ \text{ or }\ \nabla U|_{\partial\Omega}\cdot\vec{n}=g, \tag{3.8}$$

where $\breve{\rho}$ is the charge density, $f$ is the Dirichlet fixed potential and $g$ is the Neumann fixed flux boundary condition. A solution to Poisson's equation can be formed from a Green's function approach.

### 3.2.1 Green's function

Let $G(\overline{x}|\overline{x}_0)$ be the free space Green's function for the Laplace operator, which is the solution to

$$\triangle G = \delta(\overline{x}_0 - \overline{x}), \tag{3.9}$$

where $\overline{x} = (x,y)$ is a boundary point and $\bar{x}_0$ is a point on the interior of the domain. In two dimensional coordinates, the function becomes

$$G = -\frac{1}{4\pi}\ln\left\{(x_0-x)^2+(y_0-y)^2\right\}. \tag{3.10}$$

Using Green's $2^{nd}$ identity to relate the surface to the boundary flux,

$$\int\int_A (D\triangle E - E\triangle D)dA = \oint (D\bigtriangledown E - E\bigtriangledown D)\cdot\vec{n}dS \tag{3.11}$$

and replacing $D$ by the Greens function $G$ and $E$ by the potential $U$ gives

$$\int\int_A G\frac{\breve{\rho}(\overline{x})}{\epsilon_0}dA - U(\overline{x}_0) = \oint (G(\partial_{\vec{n}}U) - U(\partial_{\vec{n}}G))\cdot\vec{n}dS, \tag{3.12}$$

where $\partial_{\vec{n}}x = \nabla x\cdot\vec{n}$. Since we do not have any internal charge in a perfect conductor, $\breve{\rho}(\overline{x}_0) = 0$ and the potential at any point can be calculated from the boundary flux and potential conditions. Carefully taking the limit from the inside of the domain to the boundary of the single and double layer potential gives Eq. (3.13) [22]

$$\beta U(\overline{x}_0) = \oint_{\partial\Omega} U(\overline{x})\partial_{\vec{n}}G(\overline{x}|\overline{x}_0)\,\mathrm{d}s - \oint_{\partial\Omega}\partial_{\vec{n}}U(\overline{x})G(\overline{x}|\overline{x}_0)\,\mathrm{d}s, \tag{3.13}$$

where $\partial\Omega$ consists of a mixture of $U(\overline{x})$ along Dirichlet ($\partial\Omega_D$) and $\partial_{\vec{n}}U(\overline{x})$ along the Neumann ($\partial\Omega_N$) boundary conditions, $\partial\Omega = \partial\Omega_D + \partial\Omega_N$, and $\beta(x)$ is $1/2$ or $1$ if $x\in\partial\Omega_D$ or $x\in\partial\Omega_N$ respectively.

### 3.2.2 Numerical discretization of the problem

Approximating the potential and flux of each panel as being a $C^{-1}$ constant over the $M_k$ panels along surface $ds$ gives the following approximation:

$$\begin{aligned}
\oint_{\partial\Omega_k} U(\overline{x})\partial_n G(\overline{x}|\overline{x}_0)\,\mathrm{d}s &\doteq \sum_{i=1}^{M_k} U(\overline{x}_i)\oint_{\partial\Omega_i}\partial_n G(\overline{x}|\overline{x}_0)\,\mathrm{d}s,\\
\oint_{\partial\Omega_k}\partial_{\vec{n}}U(\overline{x})G(\overline{x}|\overline{x}_0)\,\mathrm{d}s &\doteq \sum_{i=1}^{M_k}\partial_{\vec{n}}U(\overline{x}_i)\oint_{\partial\Omega_i} G(\overline{x}|\overline{x}_0)\,\mathrm{d}s.
\end{aligned} \tag{3.14}$$

The assumption of a perfect conductor means that the electrode and needle have a fixed potential throughout. Therefore, changing the panels from constant $C^{-1}$ to linear $C^0$ potential representations may not increase the accuracy of the approach.

Inserting Eq. (3.14) into Eq. (3.13) gives the full descriptive integrals for both boundary types. The first term represents a Dirichlet boundary condition and the second a Neumann one. The terms $U(\overline{x}_0)$ and $\frac{\partial U(\overline{x}_0)}{\partial n_0}$ in the expansion arise from the effect of a panel on itself.

If $\overline{x}$ is on the boundary, then the discrete form of Eq. (3.13) is

$$\begin{aligned}\beta U(\overline{x}_0) = &\sum_{i=1}^{M_D} U(\overline{x}_i) \oint_{\partial\Omega_{D,i}} \partial_{n,0} G(\overline{x}_i|\overline{x}_0)\,\mathrm{d}s + \sum_{j=1}^{M_N} U(\overline{x}_j) \oint_{\partial\Omega_{N,j}} \partial_{\vec{n},j} G(\overline{x}_j|\overline{x}_0)\,\mathrm{d}s \\ &+ \sum_{i=1}^{M_D} \partial_{\vec{n},i} U(\overline{x}_i) \oint_{\partial\Omega_{D,i}} G(\overline{x}_i|\overline{x}_0)\,\mathrm{d}s + \sum_{j=1}^{M_N} \partial_{\vec{n},j} U(\overline{x}_j) \oint_{\partial\Omega_{N,j}} G(\overline{x}_j|\overline{x}_0)\,\mathrm{d}s,\end{aligned} \tag{3.15}$$

where $M_D$ is the number of Dirichlet panels and $M_N$ is the number of Neumann panels. Note that the flux on Dirichlet and the potential on Neumann boundaries is unknown and needs to be solved, that is the $\partial_{\vec{n}} U(\overline{x})|_{\partial\Omega_D}$ and $U(\overline{x})|_{\partial\Omega_N}$ terms. Using the prior discretization and by collecting terms, the matrix can be described as in Eq. (3.16) and mathematically as Eq. (3.17):

$$\begin{bmatrix} \text{distance from one} \\ \text{panel to another} \end{bmatrix} \begin{bmatrix} \text{unknown Dirichlet} \\ \text{and Neumann BC} \end{bmatrix} = \begin{bmatrix} \text{known Neumann} \\ \text{and Dirichlet BC} \end{bmatrix}, \tag{3.16}$$

$$\begin{bmatrix} a_{1,1}..a_{1,M_D} & b_{1,1}..b_{1,M_N} \\ \hline a_{M_D,1}..a_{M_D,M_D} & b_{M_D,1}..b_{M_D,M_N} \\ \hline c_{1,1}..c_{1,M_D} & d_{1,1}..d_{1,M_N} \\ c_{M_N,1}..c_{M_N,M_D} & d_{M_N,1}..d_{M_N,M_N} \end{bmatrix} \begin{bmatrix} \partial_{\vec{n},1} U(\overline{x}_{1,1}) \\ \vdots \\ \partial_{\vec{n},1} U(\overline{x}_{1,M_D}) \\ U(\overline{x}_{2,1}) \\ \vdots \\ U(\overline{x}_{2,M_N}) \end{bmatrix} = \begin{bmatrix} \breve{\gamma}(\overline{x}_{1,1}) \\ \vdots \\ \breve{\gamma}(\overline{x}_{1,M_D}) \\ \alpha_N(\overline{x}_{2,1}) \\ \vdots \\ \alpha_N(\overline{x}_{2,M_N}) \end{bmatrix}. \tag{3.17}$$

Here, the $a_{i,j}$ represent the inter-panel distances between Dirichlet-Dirichlet types boundaries, $b_{i,j}$ are the Dirichlet-Neumann distances, $c_{i,j}$ are the Neumann-Dirichlet distances and $d_{i,j}$ describe the Neumann-Neumann distances. The right hand side of Eq. (3.17) is the known quantities in Eq. (3.15).

The actual boundaries do not have to be all Dirichlet and then all Neumann types as described above; the boundary conditions can alternate back and forth arbitrarily. The potential at any point in the domain is thus given by summing the contributions from fixed, diverse boundaries types, as in Eq. (3.15).

### 3.3 Calculating the electrostatic force

One of the main advantages of the BEM formulation of Eq. (3.17) is the direct computation of the interface force. Solving for the $\partial_{\vec{n}} V(\overline{x}_1)|_{\partial\Omega_D}$ term of the normalized test shape

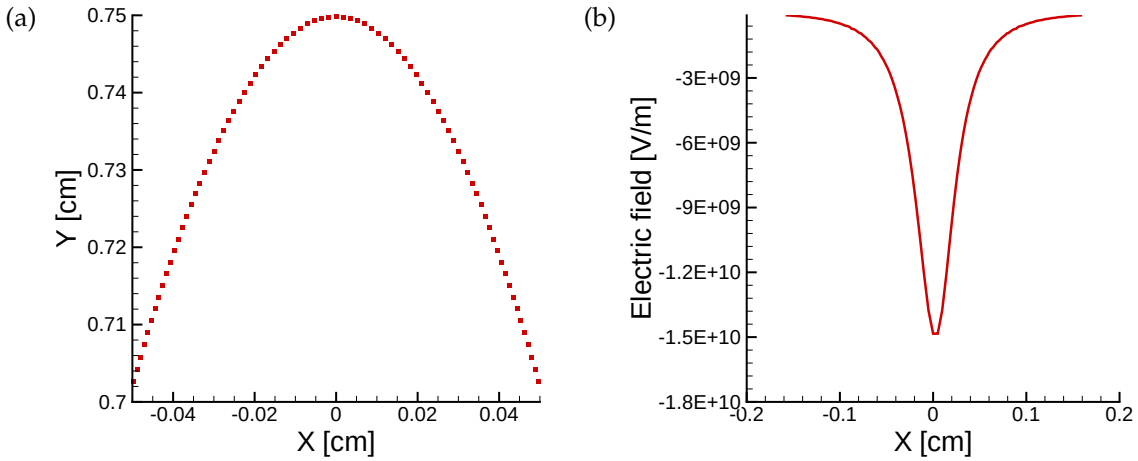


Figure 3: Boundary nodes and normal electric field along a curved surface.

in Fig. 3a provides the normal component of the electric field ($E_n$) for points in the interval $(x,y)\in[-0.05,0.05]\times[0.7,0.75]$, as seen in Fig. 3b. To calculate the electrostatic force term $qE$ in the model, consider the droplets' position. Gauss' Law states that the total flux of the electric field through an element $dA$ is given by the sum of the electric field's surface normals; this is shown in

$$UL\left[\frac{N\cdot m^2}{C}\right]=\int EdA=\oint\vec{E}\cdot\vec{n}dS=\frac{q}{\epsilon_0}, \tag{3.18}$$

where the flux is $\beta=1$ unit into the page. By drawing a box around each computational panel, the earlier assumption of a perfect conductor now implies that all electric flux is normal to the surface so $\vec{E}\equiv\vec{E}_n$ and there is no tangential electric field. Solving for the charge:

$$q=\epsilon_0 LE_n\beta. \tag{3.19}$$

As a result, the total electrostatic force experienced by the panel is given by

$$F_E[N]=qE_n=\epsilon_0 LE_n^2. \tag{3.20}$$

The electrostatic solution is computed independent of a surrounding volume grid. The calculation method for the electrical force holds for all non-crossing complex geometries, including the nesting of multiple shapes. The model is capable of determining electrostatic surface forces on a needle FEEP.

### 3.4 Surface node generation

Since BEM is a directional method, not only do all the interface locations have to be determined, but they also have to be examined sequentially. This computational task

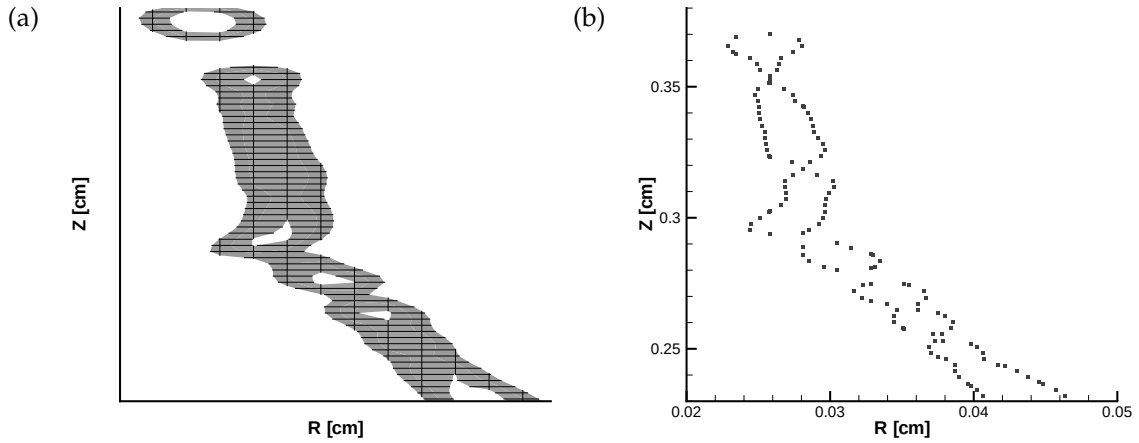


Figure 4: Surface as represented by the (a) level set variable $\phi$ from $[-0.001 \leq \phi \leq 0.001]$ and (b) surface reconstruction points.

of ordered surface node generation from level set grid data is an issue that arises often. Shape determination strongly impacts model behavior; problems in calculating the physical connectivity between panels arise from the existence of: areas of high curvature, variational spacing between located surface points, multiple surfaces, and variation in both time and space. Fig. 4 displays a situation commonly encountered that concerns surface recognition and separation of five unique droplets. In Fig. 4a, the level set variable is graphed for values $[-0.001 \leq \phi \leq 0.001]$, while the second picture displays the $\phi = 0$ locations. Fig. 5 displays the droplets along with the possible separation points. The top three drawn circles are discrete droplets; any surface tracking program has to recognize this and that droplet #5 extends over a region whose middle is necking, but not detached.

Numerous approaches for discrete shape identification were attempted before settling on a hybrid anti-crossing, tracking normal-weighting (ACTNOW) scheme. This method was created using parts of many discrete schemes in the literature. It can generate connected droplets using only $\phi$ values, including parallel lines and necking. Other alternative schemes investigated for the shape connectivity include nearest neighbor, limited distance, normal minimization, angle gradient minimization and pseudo-entropy reduction [23–27].

Starting from the top point on the midline, the ACTNOW approach traverses the level set grid vertically until the first positive $\phi$ value is encountered. The direction is then recorded, where the first instance is south. The algorithm then looks at the level set values 135 degrees counter-clockwise, or northeast originally. From there, the level set values are examined every 45 degrees to see if $\phi$ changes sign. When that sign change is identified, the new surface point is marked and the 8-point circle check is continued from the new location. In this way, a listing of the intersection points for each shape is determined. Using the list of individual droplet nodes, the order of points is determined

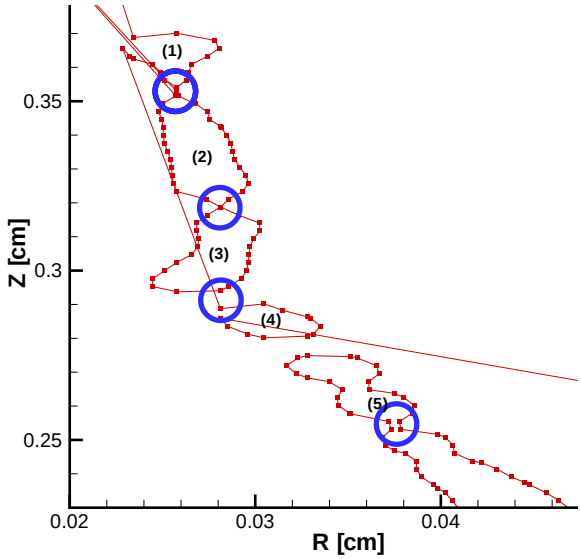


Figure 5: Individual droplets with circled potential detachment locations.

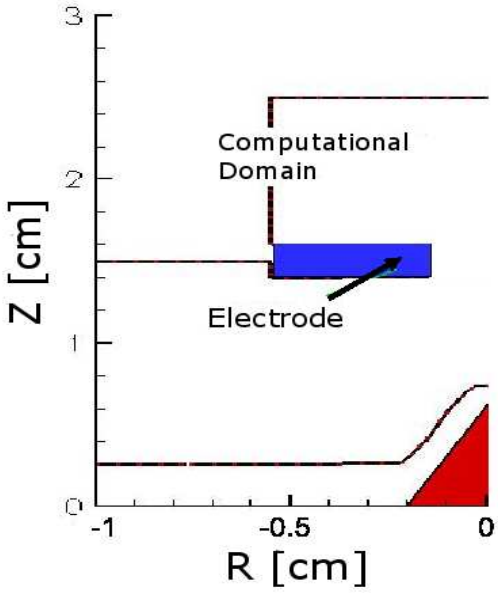


Figure 6: Computational domain, 2D axisymmetric case.

using a combination of all the prior methods. If two lines cross when linking nodes, a connection between two nodes was mistakenly drawn, and the process for that particular shape is begun again, with that connection no longer possible. The most successful sub-techniques used in ACTNOW include limiting the length of the proposed connection

near the average of the other connections and restricting the interior angle change from one point to the next.

### 3.5 Numerical verification and analysis

To verify the numerical stability of the methods against perturbations, multiple steps were taken. The simulated computational domain is shown in Fig. 6. Refining the level set mesh from $256^2$ to $2{,}506^2$ cells and lowering the top panel from $y$=2.6 cm to $y$=1.5 cm showed no change in potential contours at the needle tip or the eventual evolved shape.

Convergence in the volume loss simulations is shown in Fig. 7. Convergence is demonstrated above the 256 node level, at a cell length of 12 $\mu m$. The instantaneous calculation of the shape area with varying grid densities in Fig. 8 demonstrates the method's second-order accuracy as the error drops two decades for each order of magnitude increase in the number of nodes.

In addition, the combined method is more stable than the boundary element method alone. Dynamic time steps are chosen through a reduced CFL number stricture based on the locally smallest cell size. On its own, BEM requires (1) computational surgery when droplets form. The new shape has to be defined as a new surface and not just an extension of the previous one. In addition, the method also requires (2) a point redistribution step for panel locations to equalize relative lengths, thereby reducing numerical noise. In our implementation, the nodes are derived from the level set function at each time step, thereby avoiding both aspects (1) and (2). The level set creates these nodes by assuming symmetry about the axis. The points $(x,y)$ and $(2x_{axis}-x,y)$ are then added as surface points. The adaptive cell size and panel lengthes were limited to be at most one tenth the diameter of the tracked droplets.

An example of an intermediate step in the surface evolution in Fig. 9 presents a snapshot of the liquid surface evolution, showing both adaptive mesh refinement boxes and instantaneous velocity vectors. The run time to generate a hundred detached droplets. using a 2 GHz single-CPU machine with 2 GB of RAM was 10 minutes for the coarse grid, 2 hours for the 128x256 grid, 15 hours for the converged grid spacing of Fig. 7 and 40 hours for the finest grid.

## 4 Illustrative results

Using Eq. (3.20), the force on the surface can be calculated and then the droplets advected forward in time with Eq. (3.1), with the corresponding droplet formation varying in space and time. The needle field emitter uses indium propellant at 453 $K$, with a viscosity of 0.0017 $N\cdot s/m^2$, a surface tension of 0.552 $N/m$ and an electric field magnitude of 10 $V/nm$ at the tip [2,3]. The simulation shows the fluid accelerating at about $1.4\times10^9\, m/s^2$, and with a maximum velocity of 6.5 $km/s$. The rectangle at the top of Fig. 6 represents the position of the ring electrode and the triangle in the bottom center is the underlying solid tungsten needle.

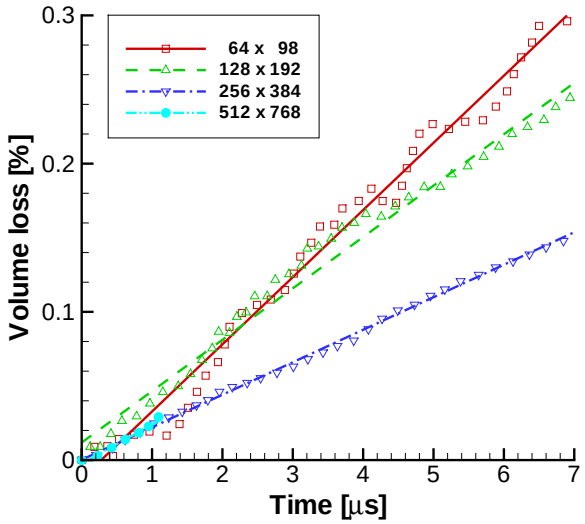


Figure 7: Volume loss over time versus level set grid density.

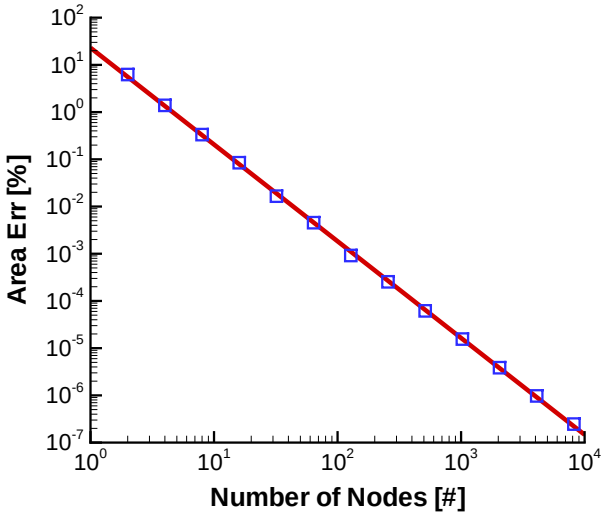


Figure 8: Area calculation error versus number of grid nodes shows a second order method.

## 4.1 Mass to charge ratio

Recording the properties of 7,600 droplets at snap off gives a mass to charge ratio distribution as seen in Fig. 10. The histogram yields a double bigaussian, showing two sub-peaks at 1,000 and 4,000 atoms/electron. The simulated MTCR of 3,900 in Fig. 10 is in agreement with that measured experimentally. Fehringer found the most common sized droplet had a radius of 0.04 $\mu$m [28]. Charged to the Rayleigh limit, those droplets

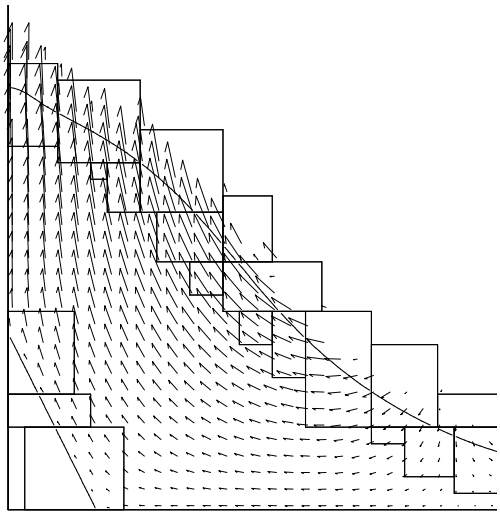

Figure 9: Indium surface evolution with adaptive mesh refinement boxes and overlaid velocity vectors.

have $q=\sqrt{64\pi^2\epsilon_0\sigma r^3}/e=2{,}774$ charges. The number of indium atoms is determined by

$$\begin{aligned}&\#\text{in. atoms}=\rho A_b(MW)_{in}\\&=(7300)\left\langle\frac{4}{3}\pi(4\times10^{-8})^3\right\rangle\left\langle\frac{1\text{amu}}{1.6606\times10^{-27}kg}\right\rangle\left\langle\frac{1\text{molecule}}{114.818\text{amu}}\right\rangle=1.026\times10^7.\end{aligned}\tag{4.1}$$

Dividing the number of atoms by the number of charges results in an experimental needle FEEP MTCR of 3699 [mol/charge].

## 4.2 Satellite droplets

When droplets form from the tip of a FEEP, smaller satellite droplets also commonly form. The electric field directly impacts the formation and fate of these secondary droplets. The field influences the volume of these satellite droplets by modulating snap off speed and the distribution of surface charge on the satellite droplets, the primary drop and the liquid remaining on the needle. These satellite droplets have larger relative charge [29], forming the smaller MTCR hump shown in Fig. 10. An example detachment location is shown in Fig. 11a, where five droplets have detached from the surface. The variation in area of the new droplets is analogous to a faucet, where a large droplet is frequently followed by a small one. Whether electrostatically charged or not, this trend of oscillating size of detached areas is common in droplet formation [30]. Fig. 11b displays the area of sequentially created droplets at one location. The substantial changes in droplet area occur from a large volume to a small volume and vice versa, in agreement with MTCR predictions.

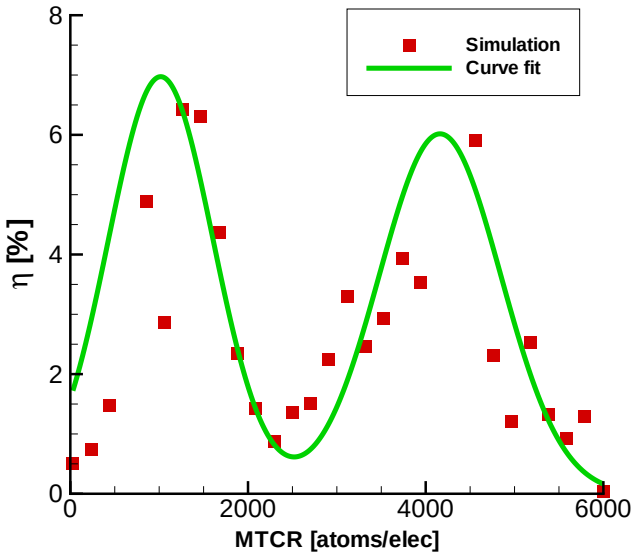


Figure 10: Droplet mass to charge probability density distributions at snap off.

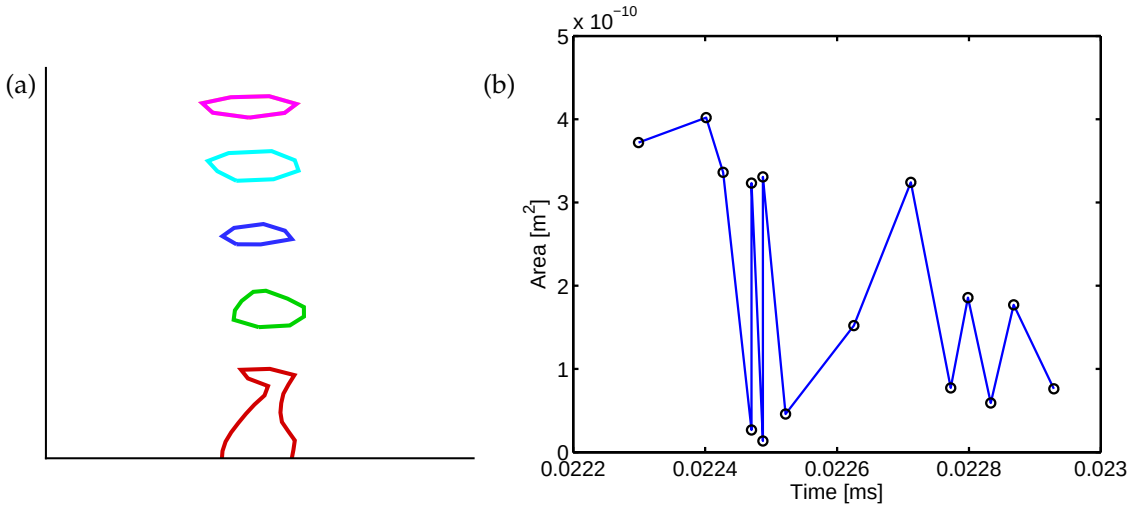


Figure 11: Droplets (a) detaching from a jet and (b) area at initial detachment. The abrupt spiking from large to small droplets is consistent with experiments.

The claim of the satellite droplets being largely the low MTCR population and therefore having greater relative charge is supported via Fig. 12. The greatest number of charges per cubic meter is for the smallest diameter droplets. As the droplet diameter increases, the Rayleigh limit caps the number of electrons on the surface, with greater diameters having a lower maximum volumetric charge before Coulombic fission occurs. The large number of droplets with a diameter around 2.5 $\mu m$ represent the MTCR mode of 3,900 presented earlier.

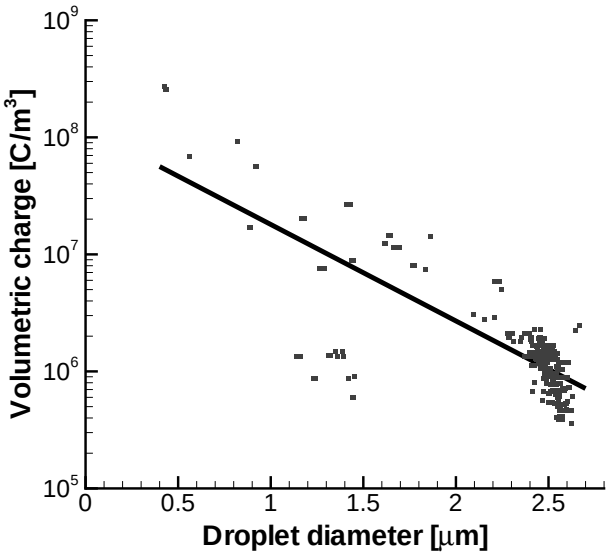


Figure 12: Droplet volumetric charge density versus diameter. The smallest satellite droplets are much more highly charged.

### 4.3 Pre-snap off shape

Suvorov presented a self-similar numerical simulation of a perfectly conducting fluid [31]. He modeled the equations of motion using electrohydrodynamics, simulating a field emitter surface evolving up to the full Taylor cone angle. Fig. 13 displays his and our work side by side for comparison; note that the EHD method only tracks the surface until the Taylor cone angle is reached. Electric field, position, surface tension and viscosity were matched, producing models that are similar in space and time. The external surface location was recorded at 81, 104, 116 and 123 ns in the EHD simulation. The BEM simulation shape occurred at 91, 120, 130 and 150 ns.

Fig. 14 presents the angle of the surface $\chi(r)$, measured from vertical to the surface tangent. A fluid peak on the order of $50\mu m$ in diameter forms and becomes more pronounced over time. As time increases, $\chi(50\mu m)$ continues to decrease as the surface becomes more vertical and droplet necking begins. This is the initiation point for the first droplet detachment.

### 4.4 Post-snap off radial spread

The PDF simulation results in Fig. 10 have shown a large MTCR frequency in the droplets around 4,000 indium atoms per electron. The following subsection attempts to support this finding by presenting a simple model that relates an observed droplet angular spread to the relative charge necessary to cause this distribution. The MTCR of this order-of-magnitude analysis was found to approximate the simulation maximum probability value.

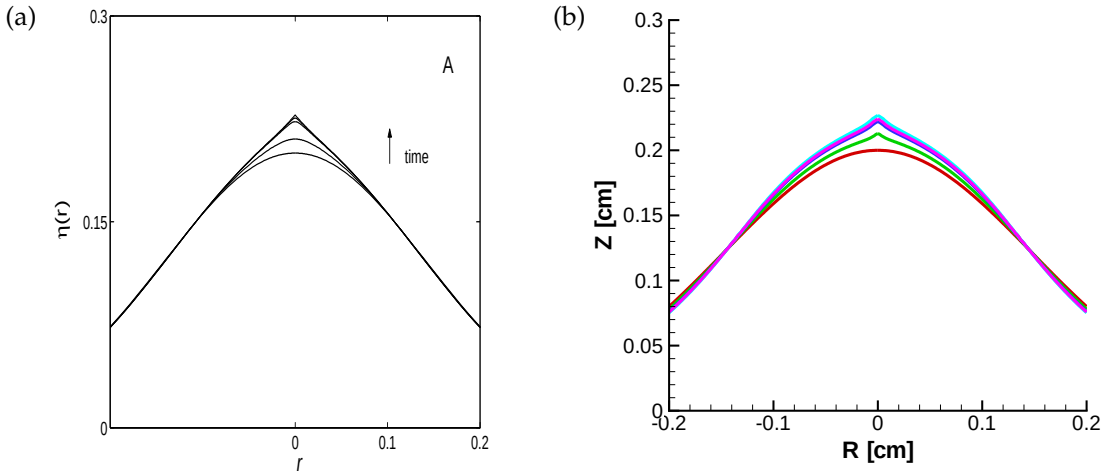


Figure 13: Centerline tip formation due to field emission by (a) Suvorov's electrohydrodynamic and (b) our boundary element methods.

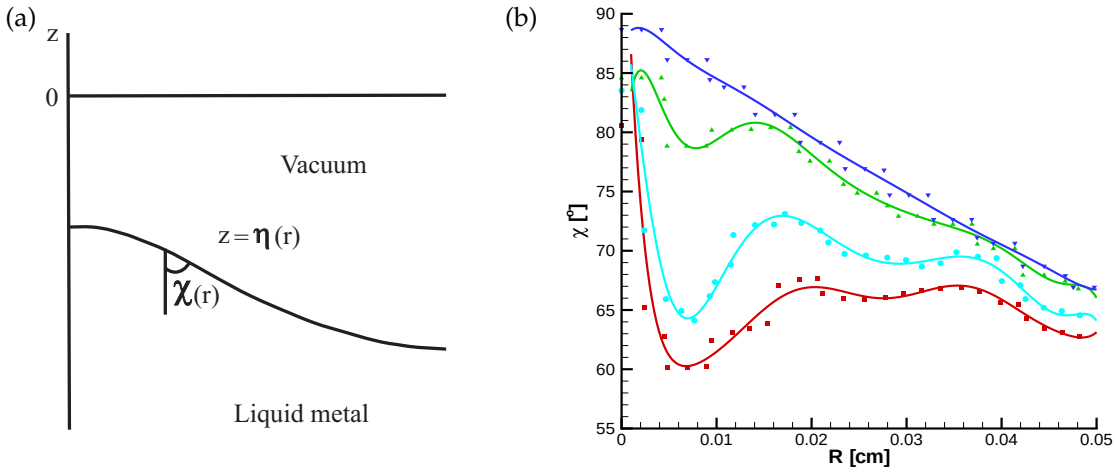


Figure 14: Angle $\chi(r)$ (a) defined from vertical to tangent to the surface and (b) plotted versus radial distance. At increasing time the angle decreases as the droplet necks.

For a droplet to be deflected in flight, it has to experience a repulsive force. Fig. 15 shows an experimental set up that records the angular density and volume of droplets from a FEEP. The axial vertical velocity $u$ of the droplet after passing the shutter is constant and is a function only of its relative charge. The off-axis horizontal velocity $v$ is a function of average acceleration $\overline{a}$ and time, or $v=\overline{a}t$. Inserting the experimental distances, the necessary acceleration and horizontal velocity for a charged droplet to reach the collection ring at an angle $\Psi$ are described by Eq. (4.2):

$$\overline{a}\left[\frac{m}{s^2}\right]=5.948\times10^7\,(\tan\Psi\sec\Psi)\left(\frac{q}{m}\right),\quad v\left[\frac{m}{s}\right]=2181(\tan\Psi)\sqrt{\frac{q}{m}}. \tag{4.2}$$

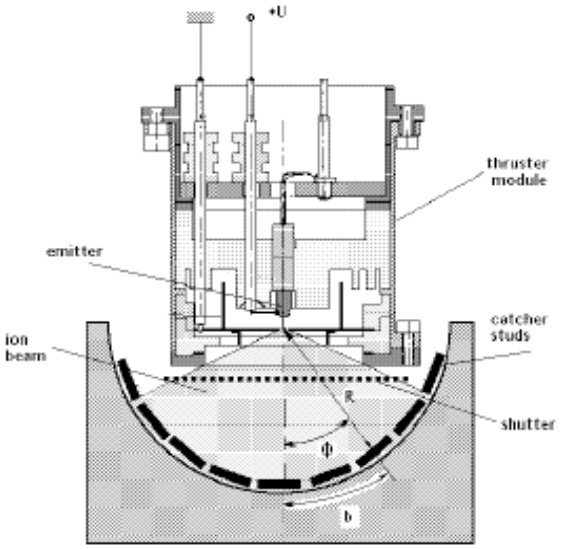


Figure 15: ARCS droplet angular measurement apparatus.

At a current of 250 $\mu A$ and an mean offset of 16.6°, half of the total droplet volume is closer to the axis and half is further away. This angular density spread can be caused by droplets that are relatively charged to the $\mathcal{O}(4000)$ indium atoms per electron predicted by the full BEM/LS hybrid approach. The model uses the equality $qE=F=\dot{m}\overline{a}$, the electrostatic repulsion as the square of the distance between droplets and the fact that the average value of the function

$$\overline{\int_{r_i}^{r_f}\frac{1}{r^2}dr}=\frac{1}{(r_f-r_i)^2}.$$

The model prediction was based on the mass of the $j^{th}$ droplet being much less than the overall mass flux $\dot{m}_{tot}$. The electric field $E_j$ from the $N_d$ detached drops is then given by Eq. (4.3), where $MTCR$ is the number of indium atoms per electron in the droplets:

$$\begin{aligned}E_j=&k\sum_{i=1,i\neq j}^{N_d}\frac{q_i}{r_i^2}=k\dot{m}\frac{8.403\times10^5}{MTCR}\sum_{i=1,i\neq j}^{N_d}\frac{1}{r_i^2}\\=&\frac{1.230\times10^9}{MTCR}\sum_{i=1,i\neq j}^{N_d}\frac{1}{r_i^2}=7.687\times10^{11}/MTCR.\end{aligned}\tag{4.3}$$

Setting the electric field $E_j=\dot{m}\overline{a}/q$ from Eq. (4.2), the relative charge of the droplets at the angle $\Psi$ can be determined. The rudimentary calculation for the MTCR needed to cause the measured mean beam spread is then given in Eq. (4.4). This simplistic model is remarkably close to the relative charge of 3,900 predicted with the BEM/LS approach and is derived solely from the average droplet relative charge needed to match a given

experimental angular dispersion:

$$MTCR_{model}\left[\frac{\#atoms}{e^-}\right] = 8{,}700. \tag{4.4}$$

# 5 Conclusion

The coupling of the boundary element and level set methods allowed for the simulation of high conductivity liquid metal droplets from a field emission thruster tip. This combination avoided many of the obstacles of modeling detaching surfaces while rapidly providing 2nd-order accurate results through reducing the electric field calculation domain. The boundary element method provided a direct solution of the external potentials and normal electric fields, thereby driving the liquid's evolution. Level sets allowed arbitrary surface geometries and the joining and separation of droplets while not requiring manual boundary modification each time step.

Validation against two independent sources was performed. Pre-snap off surface movement matches an EHD model, while post snap off relative charge for off-axis particle spread agreed qualitatively and quantitatively with that expected for droplets with a mean MTCR between 1,600-40,000. The full LS/BEM hybrid model's predicted relative charge maximum is comfortably in this range. The simulation performed significantly beyond liquid detachment without having to restart, reflecting a robust modeling method.

# Acknowledgments

The first author thanks the NASA Jet Propulsion Laboratory for funding through the NASA Graduate Student Research Program. Sussman's work supported in part by the NSF under contract DMS 0108672. Christlieb's work supported in part by the Air Force Office of Scientific Research (AFOSR) under Grant FA9550-05-1-0199.

### References

[1] M. Paine and S. Gabriel, A micro-fabricated colloidal thruster array, AIAA 2001-3329, 37th AIAA Joint Propulsion Conference, Salt Lake City, Utah, 8 July 2001.

[2] A. Genovese, M. Tajmar and W. Steiger, Indium FEEP endurance test: Preliminary results, IEPC-01-289, IEPC 27th International Electric Propulsion Conference, Pasadena, CA, October 2001.

[3] M. Tajmar, K. Marhold and S. Kropatschek, Three-dimensional In-FEEP plasmadiagnostics, IEPC 28th International Electric Propulsion Conference, Toulouse, France, July 2003, pp. 1-10.

[4] A. Genovese, W. Steiger and M. Tajmar, Indium FEEP microthruster: Experimental characterization in the 1-100 $\mu$N range, AIAA 2001-3788, 37th Joint Propulsion Conference, 8-11 July 2001, pp. 1-12.

[5] G. I. Taylor, Disintegration of water drops in an electric field, in: Proceedings of the Royal Academy of London, vol. A280, 1964, pp. 383.
[6] S. Osher and J. Sethian, Fronts propagating with curvature dependent speed: Algorithms based on Hamilton-Jacobi formulations, J. Comput. Phys., 79 (1988), 12-49.
[7] C. Nave, HyperPhysics, Dept. Physics and Astronomy, Georgia State University, Atlanta, GA 30303, http://hyperphysics.phy-astr.gsu.edu/hbase/hph.html
[8] S. Chen, B. Merriman, S. Osher and P. Smereka, A simple level set method for solving Stefan problems, J. Comput. Phys., 135 (1997), 8-29.
[9] H. K. Zhao, T. Chan, B. Merriman and S. Osher, A variational level set approach to multiphase motion, J. Comput. Phys., 127 (1996), 179-195.
[10] R. Fedkiw, T. Aslam, B. Merriman and S. Osher, A non-oscillatory Eularian approach to interfaces in multimaterial flows (the ghost fluid method), J. Comput. Phys., 152(2) (1999), 457-492.
[11] D. Peng, B. Merriman, S. Osher, H. K. Zhao and M. Kang, A PDE-based fast local level set method, J. Comput. Phys., 155 (1999), 410-438.
[12] M. Sussman, A second order coupled level set and volume-of-fluid method for computing growth and collapse of vapor bubbles, J. Comput. Phys., 187 (2003), 110-136.
[13] M. Lappa, A CFD level-set method for soft tissue growth: Theory and fundamental equations, Biomechanics, 38 (2005), 185-190.
[14] W. J. Rider and D. B. Kothe, Reconstructing volume tracking, J. Comput. Phys., 141 (1998), 112-152.
[15] M. Sussman, P. Smereka and S. Osher, A level set approach for computing solutions to incompressible two-phase flow, J. Comput. Phys., 114 (1994), 146-159.
[16] M. Ohta, S. Haranaka, Y. Yoshida and M. Sussman, Three-dimensional numerical simulations of the motion of a gas bubble rising in viscous liquids, J. Chem. Eng. Jpn., 37(8) (2004), 968-978.
[17] M. Sussman, K. M. Smith, M. Y. Hussaini, M. Ohta and R. Zhi-Wei, A sharp interface method for incompressible two-phase flows, J. Comput. Phys., 221 (2007), 469-505.
[18] M. Sussman, E. Fatemi, P. Smereka and S. Osher, An improved level set method for incompressible two-phase flows, Comput. Fluids, 27 (1998), 663-680.
[19] S. K. Godunov, A. V. Zabrodin and G. P. Prokopov, A difference scheme for two-dimensional unsteady aerodynamics and an example of calculations with a separated shock wave, J. Comput. Math. Math. Phys., 2(6) (1961), 1020-1050.
[20] M. Sussman, A parallelized, adaptive algorithm for multiphase flows in general geometries, Comput. Struct., 83 (2005), 435-444.
[21] M. Sussman and E. Puckett, A coupled level set and volume-of-fluid method for computing 3D and axisymmetric incompressible two-phase flows, J. Comput. Phys., 162 (2000), 301-337.
[22] G. Folland, Introduction to Partial Differential Equations, Princeton University Press, 1979.
[23] N. Amenta, S. Choi, T. K. Dey and N. Leekha, A simple algorithm for homeomorphic surface reconstruction, J. Comput. Geom. Appl., 12 (2002), 125-141.
[24] J. Bloomenthal, Polygonisation of implicit surfaces, Comput. Aided Geom. Design, 5(4) (1988), 341-355.
[25] D. Enright, S. Marschner and R. Fedkiw, Animation and rendering of complex water surfaces, in: Proceedings of ACM SIGGRAPH, 2002, pp. 736-744.
[26] W. E. Lorensen and H. E. Cline, Marching cubes: A high resolution 3D surface construction algorithm, in: Computer Graphics (Proceedings of SIGGRAPH 87), vol. 21, no. 4, July 1987, pp. 163-169.

[27] S. Osher and R. Fedkiw, Level set methods and dynamic implicit surfaces, in: S. Antman (Ed.), Applied Mathematical Sciences, Springer, vol. 153, 2003.
[28] M. Fehringer, F. Rudenauer and W. Steiger, Ultra-precise indium thruster, wp 2000: Droplet emission, Seiborsdorf, Austria, Tech. Rep. ESTEC Contract No. 12376/97/NL/PA, 2000.
[29] R. Grimm and J. L. Beauchamp, Dynamics of field-induced droplet ionization: time-resolved studies of distortion, jetting, and progeny formulation from charged and neutral methanol droplets exposed to strong electric fields, J. Phys. Chem. B, 109 (2005), 8244-8250.
[30] X. Zhang and O. A. Basaran, Dynamics of drop formation from a capillary in the presence of an electric field, J. Fluid Mech., 326 (1996), 239-263.
[31] V. Suvorov and E. Litvinov, Dynamic taylor cone formation on liquid metal surface: numerical modelling, J. Phys. D Appl. Phys., 33 (2000), 1245-1251.